Time-Lapse Monitoring of Daily Velocity Changes in Binchuan, Southwestern China, Using Large-Volume Air-Gun Source Array Data

Yi Luan[1], Hongfeng Yang[*1,2] , Baoshan Wang[3,4] , Wei Yang[4,5], Weitao Wang[4,5], Jun Yang[6], and Xiaobin Li[6]

Abstract

Temporal changes of seismic velocities in the Earth's crust can be induced by stress perturbations or material damage from reasons such as strong ground motion, volcanic activities, and atmospheric effects. However, monitoring the temporal changes remains challenging, because most of them generally exist in small travel-time differences of seismic data. Here, we present an excellent case of daily variations of the subsurface structure detected using a large-volume air-gun source array of one-month experiment in Binchuan, Yunnan, southwestern China. The seismic data were recorded by 12 stations within ∼ 10 km away from the source and used to detect velocity change in the crust using the deconvolution method and sliding window cross-correlation method, which can eliminate the "intercept" error when cutting the air-gun signals and get the real subsurface variations. Furthermore, the multichannel singular spectral analysis method is used to separate the daily change (∼ 1 cycle per day) from the "long-period" change (< 1 cycle per day) or noise. The result suggests that the daily velocity changes at the two nearest stations, 53277 (offset ∼ 700 m) and 53278 (offset ∼ 2.3 km), are well correlated with air temperature variation with a time lag of 5.0 ± 1.5 hr, which reflects that the velocity variations at the subsurface are likely attributed to thermoelastic strain. In contrast, both daily and long-period velocity changes at distant stations correlate better with the varying air pressure than the temperature, indicating that the velocity variations at deeper depth are dominated by the elastic loading of air pressure. Our results demonstrate that the air-gun source is a powerful tool to detect the velocity variation of the shallow crust media.

Introduction

Knowledge of the stress field and how it evolves over a broad spectrum of time scale is important for the understanding of crustal tectonics and mechanics of the earthquake cycle (Li *et al.*, 2003; Brenguier *et al.*, 2008; Niu *et al.*, 2008; Yang *et al.*, 2014, 2021; Yang, 2015). A number of laboratory and field studies have shown that the seismic-wave velocities of crustal rocks are sensitive to stress, which suggests the possibility of inferring stress changes by measuring the corresponding changes of seismic velocities, provided that we can isolate the contribution of stress to the observed velocity change and have a dependable calibration of the relationship between them (Birch, 1960, 1961; Nur, 1971; Reasenberg and Aki, 1974; Leary *et al.*, 1979; Yamamura *et al.*, 2003). Accordingly, there are two challenges. First, the daily and hourly changes of seismic velocities are subtle and have to be measured with field instrumentation that can provide high temporal and spatial precision. Second, the velocity changes can be caused by multiple sources, including barometric pressure, temperature, and solid earth tides, and so on. Therefore, these other contributions must be identified before we can pinpoint the crustal stress contribution.

In the past two decades, significant improvements have been made in the measurement of such small velocity changes

1. Earthquake System Science Programme, The Chinese University of Hong Kong, Shatin, Hong Kong, China, https://orcid.org/0000-0002-5925-6487 (HY);
2. Shenzhen Research Institute, The Chinese University of Hong Kong, Shenzhen, Guangdong, China; 3. School of Earth and Space Sciences, University of Science and Technology of China, Hefei, China, https://orcid.org/0000-0001-7203-9703 (BW); 4. Institute of Geophysics, China Earthquake Administration, Beijing, China; 5. Key Laboratory of Earthquake Source Physics, China Earthquake Administration, Beijing, China; 6. Earthquake Agency of Yunnan Province, Kunming, China

*Corresponding author: hyang@cuhk.edu.hk

using either passive or active sources. The passive sources include repeating earthquakes (e.g., Haase *et al.*, 1995; Schaff and Beroza, 2004; Peng and Ben-Zion, 2006) and ambient seismic noise (e.g., Sens-Schönfelder and Wegler, 2006; Brenguier *et al.*, 2008, 2014; Mordret *et al.*, 2016; Liu *et al.*, 2021). Repeated seismic tomography has also been used (e.g., Patanè *et al.*, 2006; Julian and Foulger, 2010; Koulakov and Vargas, 2018). These passive sources have been very effective for the detection of relatively large velocity changes, such as those induced by earthquakes with magnitude larger than 5 (Li *et al.*, 1998; Patanè *et al.*, 2006; Chen *et al.*, 2010). However, they have two limitations. First, these methods usually need observations over a long duration (Niu *et al.*, 2003). Second and the most critical in the present context, when it comes to measuring subtle variations of seismic velocity, these methods have difficulties, mainly due to poor temporal sampling and thus less accuracy (Hadziioannou *et al.*, 2011).

Active sources are artificial seismic sources, including a vibrator, controlled explosion, electric hammer, air gun, and piezoelectric transducer (Yamamura *et al.*, 2003; Schaff and Beroza, 2004; Silver *et al.*, 2007; Niu *et al.*, 2008; Wang *et al.*, 2008; Chen *et al.*, 2014). If the origin time and location are precisely known and have high repeatability, then such active sources can potentially resolve subtle variations with both high temporal and spatial resolutions. In particular, using an electric hammer as a source to generate repeated seismic waves, Wang *et al.* (2008) conducted a one-month field experiment near the Xiaojiang fault zone in Yunnan, China. Five short-period seismometers were deployed at ~10 m to 1.2 km away from the source. From this experiment, they were able to resolve subtle temporal variations on two different time scales: a long-term linear trend as well as daily cycles, which were interpreted as the velocity response to the barometric pressure. Yang *et al.* (2018) reported an experiment using a borehole air-gun source recorded by nine short-period seismometers at distance of ~3–900 m in the east of Xiaojiang fault zone in Yunnan, China. Their results showed a good correlation between observed velocity change and groundwater-level change of several meters. However, because the utilized sources in their research (e.g., hammer or one 250 inch^3 air gun) cannot excite signals that can be recorded at larger distances, the spatial coverage was limited. Later, Wang *et al.* (2020) derived the *P*- and *S*-wave velocity changes using the air-gun source in Binchuan, Yunnan Province, with a one-week experiment. They found that thermoelastic strain was the primary cause to explain the ~3 hr delay between seismic-velocity change and temperature but was unable to explain the full amplitude of the velocity change. Liu *et al.* (2021) investigated seasonal velocity changes from the same air-gun source, and, however, found that they were largely affected by the water-level changes in the reservoir where the air guns are located.

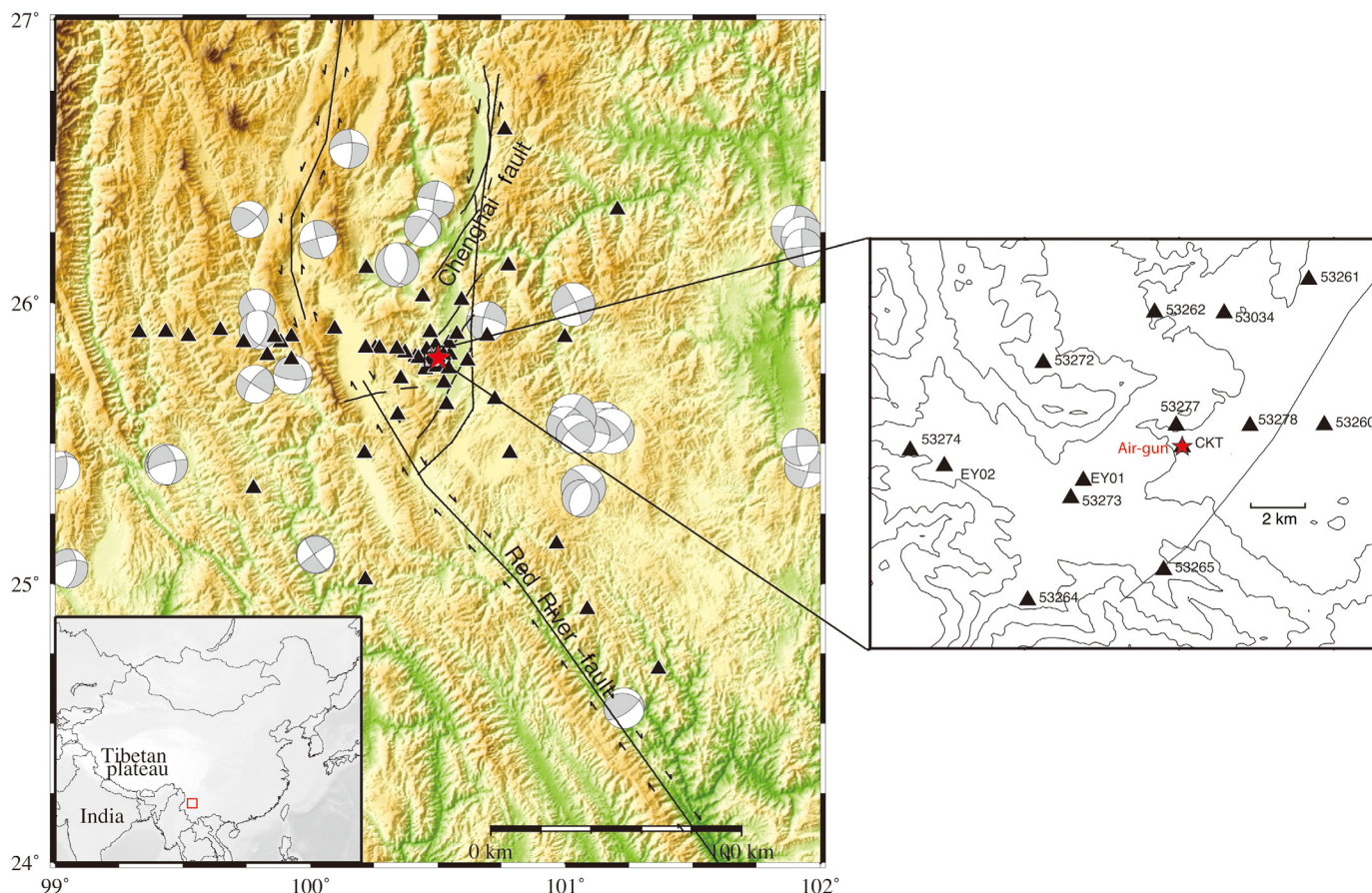The limitations of the most related studies are either too short in the spatial length of the stations or too sparse in the time interval between measurements, making it hard to detect the subsurface changes at a regional scale. In this study, by overcoming these drawbacks, we conducted a study at the Binchuan Fixed Airgun Signal Transmission Station (FASTS), based on an air-gun array with four volumes of 2000 inch^3, located in west Yunnan (Wang *et al.*, 2012). The Binchuan FASTS has the unique capability to measure the relative temporal change in seismic velocities with a precision better than 10^{-4} (Wang *et al.*, 2020). The air gun was activated approximately once per hour during the one-month experiment in 2015. The seismic network, which consists of 12 seismic stations within 10 km from the source, is capable of high-resolution local-scale detection in field experiments.

Having captured the spatiotemporal changes in velocities, we need to isolate the contribution of stress from those of barometric pressure, temperature, and solid earth tides. Because these time series have a range of characteristic frequencies, it is a significant challenge to identify the individual contributions in the analysis of climatic and velocity change (Keppenne and Ghil, 1993; Ghil *et al.*, 2002; Walwer *et al.*, 2016; Zhang *et al.*, 2017). The Multichannel Singular Spectrum Analysis (M-SSA) method is a principal component analysis method and an advanced technique that has been developed to tackle this challenge (Walwer *et al.*, 2016; Zhang *et al.*, 2017). In the M-SSA method, extracting the information of covariance of time series and its lagged replicates is the key idea (Ghil *et al.*, 2002; Walwer *et al.*, 2016). The main benefit of this method is that it does not require prior knowledge about the period and amplitude or the spatiotemporal structures of the time series. To our knowledge, this is the first study to apply this M-SSA method into our seismic data, to separate the velocity changes into different frequency components and associate them with the meteorological data to examine the mechanisms that govern the velocity changes. The refined time series after the M-SSA method shows more information than previous studies (Wang *et al.*, 2020).

This study is designed to tackle the two objectives of resolving subtle velocity changes and isolating the contribution of the velocity changes from multiple sources, and for the first objective, we adopted the deconvolution method to remove the intercepting time errors caused by cutting the air-gun waveforms and sliding window cross-correlation method to estimate the velocity change. For the second objective, we extracted information on different frequency components using the M-SSA method on the time series of seismic-velocity change and associated them with contributions from barometric pressure and temperature records.

Study Region and Seismic Experiments
The Binchuan FASTS
The Binchuan FASTS is located in a tectonic block bounded in the southwest by the Red River fault and in the east by the Chenghai fault (Fig. 1). The crustal thickness in the region

Figure 1. A map of Binchuan, Yunnan, showing the air-gun seismic networks (black triangles), the air-gun source (red star), and surface traces of the Red River fault system and Chenghai fault system (black lines). The stations used in this study are black triangles in the right box. Focal mechanism plots show moment tensor solutions of earthquakes with magnitudes larger than 4.5 from 2000 to 2014 in Xu *et al.* (2020). Lower inset figure shows tectonic setting in the region and the location (red box) of the study area. The color version of this figure is available only in the electronic edition.

varies from 42 to 46 km, based on receiver function results from recordings on a 2D dense array (Jiang *et al.*, 2020). The regional tectonics is associated with the collision of the Indian and Eurasian plates, and these fault systems host frequent earthquake activities and pose great regional seismic hazards, as evidenced by the 2021 M_s 6.4 Yangbi earthquake (e.g., Zhang *et al.*, 2021). The Red River fault system consists of a group of young and active faults related to an overall clockwise rotation in western Yunnan (Wang *et al.*, 1998). The Chenghai fault extends over ~200 km, and the largest historical earthquake was the 1515 **M** 7.75 Yongsheng earthquake. Yang *et al.* (2020) have deployed a dense linear array with 125 short-period stations crossing the Chenghai fault for one month in January 2018. Ambient noise tomographic results reveal a profound low-velocity zone (LVZ) with 3.4 km in width beneath the array (Yang *et al.*, 2020). The depth extent is constrained as ~1 km with clear lateral variation from a newly developed array-based receiver function technique (Jiang *et al.*, 2021). Xu *et al.* (2020) presented 1833 moment tensor solutions of small-to-moderate earthquakes in Yunnan that occurred between January 2000 and December 2014. There are 41 moment tensor solutions of earthquakes with magnitudes larger than 4.5 in our region during this period (24°~27° N, 99°~102° E) (Fig. 1). Above all, the Binchuan FASTS provides a rich dataset to analyze the subsurface changes associated with fault activities continuously.

Binchuan air-gun source

The air-gun array was composed of four air guns (firing pressure 15 MPa), which are highly efficient in energy conversion and can generate highly repeatable signals. They were towed 10 m below the water surface in the Dayindian reservoir that has an area of 2 km² and a water depth of ~17 m (Wang *et al.*, 2012; Chen *et al.*, 2017). The air-gun array was established in 2011 and continuously deployed since January 2013. Our one-month densely air-gun excitation experiment at an interval of 1 hr was from 18 November 2015. The timing of air guns was accurately controlled by synchronization to the Global Positioning System (GPS) clock. As elaborated later, the signal sampling in each receiver was also synchronized to the GPS clock.

Station distribution

Our field experiment contained 40 portable stations around the Binchuan FASTS (Fig. 1). The nearest station CKT was

deployed 50 m from the source, and the farthest station was 151 km away from the source. The stations were equipped Güralp CMG-40 T short-period sensor with the frequency band from 2 s to 100 Hz and RefTek 130B datalogger with the sampling rate of 100 samples per second. There were three broadband stations, including EY01 (offset ∼3.4 km), EY02 (offset ∼7.8 km), and 53034 (offset ∼4.7 km) using Reftek 130 recorders and Güralp-40 T with the frequency band from 30 s to 100 Hz. There were also temperature, precipitation, and barometric pressure recordings near the air-gun site. Barometric pressure, temperature, and precipitation measurements were sampled at half one hour continuously.

Air-gun signals

The signatures of air-gun signals generated in water reservoirs have been reported by various research (e.g., Ziolkowski, 1970; Reasenberg and Aki, 1974; Wang *et al.*, 2012, 2020; Chen *et al.*, 2014). As to air-gun signals of Binchuan FASTS, Chen *et al.* (2014) analyzed the characteristics of air-gun signals and the influencing factors from six experiments in April 2011, May 2011, and April 2013 based on field experiments with Binchuan FASTS. Luan *et al.* (2016) investigated the temporal variation of subsurface structure through the analysis of air-gun signals generated in the year 2013 and found four stations near the Chenghai fault showed structural changes. Besides, we also analyzed the dominant frequency (∼4 Hz) and processing procedures, including 3–5 Hz band-pass filter of Binchuan air-gun signals in Luan *et al.* (2016). The waveforms of single-shot air-gun signals in the 2015 densely excitation experiment recorded by 12 nearest stations from air-gun sources are shown in Figure S1, available in the supplemental material to this article. The apparent V_P and V_S are 4.9 and 2.6 km/s, respectively.

Methodology

The seismic-velocity changes are usually estimated by measuring the subtle changes in absolute travel time along a fixed source–receiver path (Snieder *et al.*, 2002). In addition, this method is used in our study. However, the measurement usually suffers from systematic timing errors in the digitizer's base clock and intercepting time errors. The intercepting time errors are caused by cutting the air-gun waveforms for cross correlation. Thus, first we introduce the method to estimate the relative velocity change (dv/v) and then the deconvolution method, which shows its effectiveness in removing the intercepting time errors and waveform changes caused by different air-gun excitations.

To estimate the temporal relation and assess the potential causality between any two records, former researchers used to measure the delay obtained with cross correlation from various observations. However, it is less robust and may draw a wrong conclusion when measuring the delay between some of the meteorological data (e.g., pressure and temperature) and our

dv/v time series that consists of mixed frequency component signals. Thus, in this section, we, for the first time, introduce this M-SSA method into our data. With this method, the meteorological data, as well as dv/v time series, are separated into different frequency components (i.e., long-term trend signals and different short-period periodic signals) to examine the specific mechanism that governs the velocity change.

Deconvolution to retrieve the Green's function

The air-gun console generates an excitation log during the air-gun excitation process, which records the excitation time. However, due to the influence of the air-gun control equipment clock calibration, mechanical delay, and time recording accuracy, and so on, the recorded excitation time and the real excitation time in the gun control log may differ. Therefore, we use the nearest station CKT (about 50 m from the air-gun source) as the reference station, intercepting a 100 s waveform as the template, and using the cross-correlation technique between the template and all the other waveforms of the station CKT (∼50 m) to determine the relative air-gun excitation time. Then, we use the relative air-gun excitation time to intercept 100 s waveforms of other stations. All the intercepted waveforms are deaveraged, detilted, processed, and 3–5 Hz Butterworth band-pass filtered. Finally, the recorded waveform of each hour in each station is cross correlated with the reference waveform (linear stacking of daily waveforms). The time delay is obtained corresponding to the maximum correlation coefficient. The single-shot air-gun signals recorded by stations within 10 km are shown in different colors according to the source–receiver distance. The delay time of each station is in the same color as the seismogram of that station. As shown in Figure S2, the measured delay time between the waveforms recorded at the same station is near one sampler (0.01 s). Besides, in different stations, the measured delay time coincides quite well. Because the systematic timing errors in the digitizer's base clock measured by REFTEK-130 remain in the order of a microsecond, the observed one sampler error (0.01 s) that appeared in all stations was highly possible due to the intercepting time errors when determining the origin times using correlations of the air-gun waveforms. Besides, the air-gun signals may also suffer from subtle waveform changes with different excitations.

To remove the intercepting time error and eliminate the waveform changes caused by source variation, we use the deconvolution method (Snieder *et al.*, 2006) to remove the impact of delay time drift that is not from the real subsurface variation. The most commonly employed deconvolution method is a water-level-stabilized frequency-domain method (e.g., Clayton and Wiggins, 1976), although the time-domain iterative deconvolution method is also used in other studies (Ligorría and Ammon, 1999). Because frequency-domain water-level deconvolution is better in terms of computational efficiency, thus, we choose the frequency-domain water-level
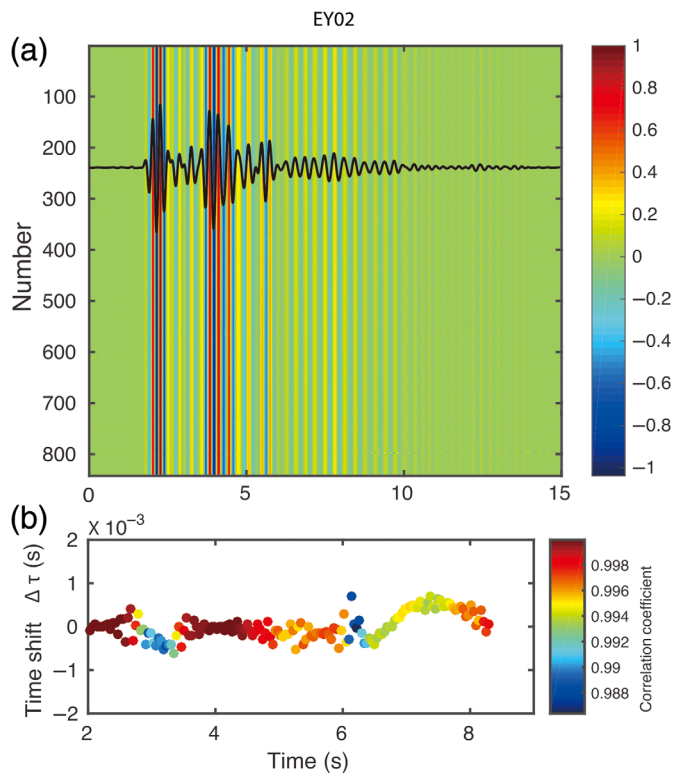
Figure 2. Relative travel-time measurements at station EY02 with source–receiver distance ~7.8 km. (a) The daily stacked seismogram on 12 November together with one month over 800 numbers' linear stacking of two consecutive seismograms using running stacking method in each day. All data are after 3–5 Hz band-pass filter. Color represents the normalized amplitude. (b) Dots represent the differences between the first shot on 12:04:59 in the 322th day of 2015 and the last shot on 01:04:59 in the 352th day of 2015. Different colors show the correlation coefficient between the two waveforms in each moving window. The color version of this figure is available only in the electronic edition.

deconvolution with the water-level factor C set as 0.0001. First, we choose the records of the near-field station CKT (~50 m) to approximate the source time function. Then, the data recorded at each station is deconvolved with the source time function for every excitation. The influence of the source is removed and obtained the Green's functions between the stations and the reference station CKT (~50 m) at the one-hour time interval.

Estimation of velocity change

The estimation of the velocity change can be retrieved from the cross correlation of the waveforms recorded before and after the change happened (Snieder *et al.*, 2002). When there is a change in the bulk velocity field, delay time dt and lapse time t will exhibit a linear relationship (e.g., Niu *et al.*, 2003; Snieder *et al.*, 2006). The fractional change of velocity, dv/v, is equal to the negative slope dt/t of the lines (i.e., $dv/v = -dt/t$). To extract the small difference dt in travel times of the waveforms from

two shots, we use the sliding window cross-correlation technique (e.g., Snieder *et al.*, 2002; Wang *et al.*, 2008). dt is given by the position of the maximum of the cross-correlation function between unperturbed and perturbed wavefields (e.g., Hillers, Ben-Zion, *et al.*, 2015). To improve the accuracy, the cosine interpolation of the calculation result is extracted to obtain the travel-time change of higher precision (Liu *et al.*, 1983). We calculated the cross correlation between each Green's function and the reference Green's function with the length of the 1 s moving window from the first arrival time of P wave; the running step of each 1 s moving window is one sampling interval (i.e., 0.01 s). Then, we choose a 0.3 s window that contains the largest correlation coefficient within each 1 s window to calculate the average dt. The reason we chose the 0.3 s window is that it approximates the one-cycled period of the air-gun waveform.

We take the station EY02 (~7.8 km) as an example in dt/t estimation. Figure 2a shows ~700 vertical-component seismograms of one month recorded by the station EY02 (~7.8 km). The time series of time shifts and correlation coefficients for the reference data (the daily stacked seismogram) and each linear stacking of two consecutive seismograms are in Figure 2b. For all the stations, the correlation coefficient values are more than 0.98 for all the time windows. The correlation coefficients become lower around 3 and 6 s in lapse time in the station EY02 (~7.8 km). Because the slope of the dt/t (i.e., the velocity variation) is not consistent, and its value depends largely on the choice of the lapse time segment. Thus, we calculated the velocity change using the mean value of the delay time with respect to the lapse time, on the condition that the cross-correlation coefficients are higher than 0.9 in the 1 s moving time windows. The precision in the delay time estimation was based on the Cramer–Rao lower bound (Carter, 1987). The detailed information can be found in Text S2.

M-SSA

The time series of relative velocity changes dv/v is influenced by long-term tectonic movement as well as atmosphere loading change, temperature change, and Earth tides (Penna and Stewart, 2003), which have either semidiurnal or diurnal periods. To estimate the temporal relation and assess the potential causality between any two records, we use the M-SSA method, which can help us to isolate signals of different frequencies that are mixed in the original time series (Ghil *et al.*, 2002; Zhang *et al.*, 2017). This method has been widely utilized in detecting and reconstructing periodic and nonperiodic GPS and gravity data (Walwer *et al.*, 2016; Zhang *et al.*, 2017). The detailed information can be found in Text S1.

We take the spatiotemporal correlation between dv/v, temperature, and air pressure data into account. Thus, we use the dv/v and temperature data to formulate a two-channel singular spectrum analysis (SSA), dv/v, and air pressure data to formulate another two-channel SSA. The dominant principal

component represents the trend that contains the largest fraction of the correlated signal. Besides, we mainly analyze the reconstructed components (RCs) using the first 10 spatio-temporal principal components and the spatiotemporal empirical orthogonal functions, which correspond to the largest 10 eigenvalues in the dv/v, temperature, and air pressure data.

To make the dv/v data applicable in the M-SSA, we interpolated the dv/v data to hourly intervals using the SSA gap-filling procedure. We obtained nearly 700 days' common daily data points from all the 12 seismic stations. We suggest that the window width of 180 days could effectively separate the semidiurnal, diurnal, long-period changes, noise, and transient signals.

Results

The results are presented in two parts. We briefly describe the general features of the temporal evolution, including the relative travel-time measurements and the delay time observed in different stations, and present a qualitative comparison with cyclic behaviors of thermal, atmospheric, hydrologic, and tidal processes. Then, we present the refined time series of velocity changes and clean periodic signals obtained with the help of the effective approach M-SSA and variation of daily velocity cycle with source–receiver distance. Quantitative correlations between velocity changes and thermal, atmospheric, and tidal processes are then discussed.

Observed velocity changes
General features of the temporal evolution. A significant daily variation of delay time is found for all stations and in the different lag time windows (Fig. 3). The measured delay time in the blue and red curves is calculated from the blue and red windows marked in the seismogram in each station. The blue and red windows are 1 and 2 s after the picked arrival time with 1 s length, respectively. In the nearest station 53277 (~700 m), the delay time in the early blue window results is not in phase with the later red window delay time (red curve in Fig. 3a2). In the nearest stations 53277 (~700 m) and 53278 (~2.3 km), the delay time results (red curve) measured from the later red window show larger amplitude and thus larger velocity change than that measured from the early blue window. In contrast, the delay time results of the farther away stations show a higher consistency between blue and red windows, which indicated very stable delay time estimates that may be from the similar subsurface medium response.

Comparison with cyclic behaviors of thermal, atmospheric, hydrologic, and tidal processes.
Figure 4a shows the altogether measurements of the velocity changes together with the error bars. We distinguish a daily cycle velocity change with the amplitude of around 0.08% for 5–10 s lag time in station 53277 (~700 m). The observed mean air temperature, barometric pressure, water level of the Dayindian reservoir,

precipitation, wind speed, and the synthetic earth solid tide over all available days (~1 month) are plotted. The temperature changes are dominated by a daily period with around 15 differences between day and night (Fig. 4b). Barometric pressure shows the dominant long-term trend and diurnal, semi-diurnal period with an amplitude of about 2 kPa (Fig. 4c). During the 1 hr densely excitation period (12:14 a.m. of 17 November to 11:05 a.m. of 18 December 2015), the water level of the Dayindian reservoir was measured changing from 22.46 to 22.89 m (Fig. 4d). The maximum water level difference of the Dayindian reservoir is around 0.4 m. The velocity change estimations resemble the pattern of the temperature. The little precipitation here is unlikely to cause the velocity change. There is a long-term decreasing trend in the observed velocity change for the whole month (Fig. 4a), which may be associated with an overall decreasing trend of temperature.

Refined time series of velocity changes from M-SSA
We apply M-SSA to the dv/v data to separate the daily signals from signals of other spectral. Taking the dv/v of broadband EY01 station (~3.4 km) as an example (Fig. 5), the result shows the first 10 RCs. The daily signals RC3 (9.07% contribution) and RC4 (8.75% contribution) are recovered, and show similar temporal variations (Fig. 6b). Besides, the long-term trend in RC1 (34.4% contribution) and RC2 (9.23% contribution) is also vital (Fig. 6a). The observed amplitude of long-term velocity change is about 1×10^{-4}, which is in the same magnitude as the daily velocity change. In addition, we find a five-day cycle in RC5 (5.1% contribution), RC6 (2.05% contribution), and RC7 (1.66% contribution) that are similar in both magnitude and phase (Fig. 6c). The other three components with less contribution are shown as RC8 (1.64%), RC9 (1.36%), and RC10 (1.34%).

Using the method of M-SSA to further extract and reproduce the daily signal, we can see that there is time shift of velocity change when choosing different windows (2–3 s and 4–5 s) in the nearest stations 53277 (~700 m) and 53278 (~2.3 km) (see Fig. S3a,b). This is similar to what was observed in Richter *et al.* (2014) that choosing different lag time windows has different phase shifts between the measurements. However, in farther away stations, the signals demonstrate a high degree of consistency for all lapse time (see Fig. S3c,d).

We compare the dv/v between different stations and find that the dv/v of the station 53277 (~700 m) with 2–3 s (2–3 s is 2 and 3 s after first arrival time) lag time window (mainly S-wave part) has a peak-to-peak daily variation with the dv/v of station 53278 (~2.3 km) with 2–3 s lag time window (Fig. 7a). Besides, if we take the dv/v of station 53273 (~3.9 km) as the reference, the dv/v of other stations share a similar pattern with that of station 53273 (~3.9 km) with only amplitude difference and no time shift (Fig. 7c–k). However, the dv/v of station 53277 (~700 m) has a phase shift compared to the dv/v of
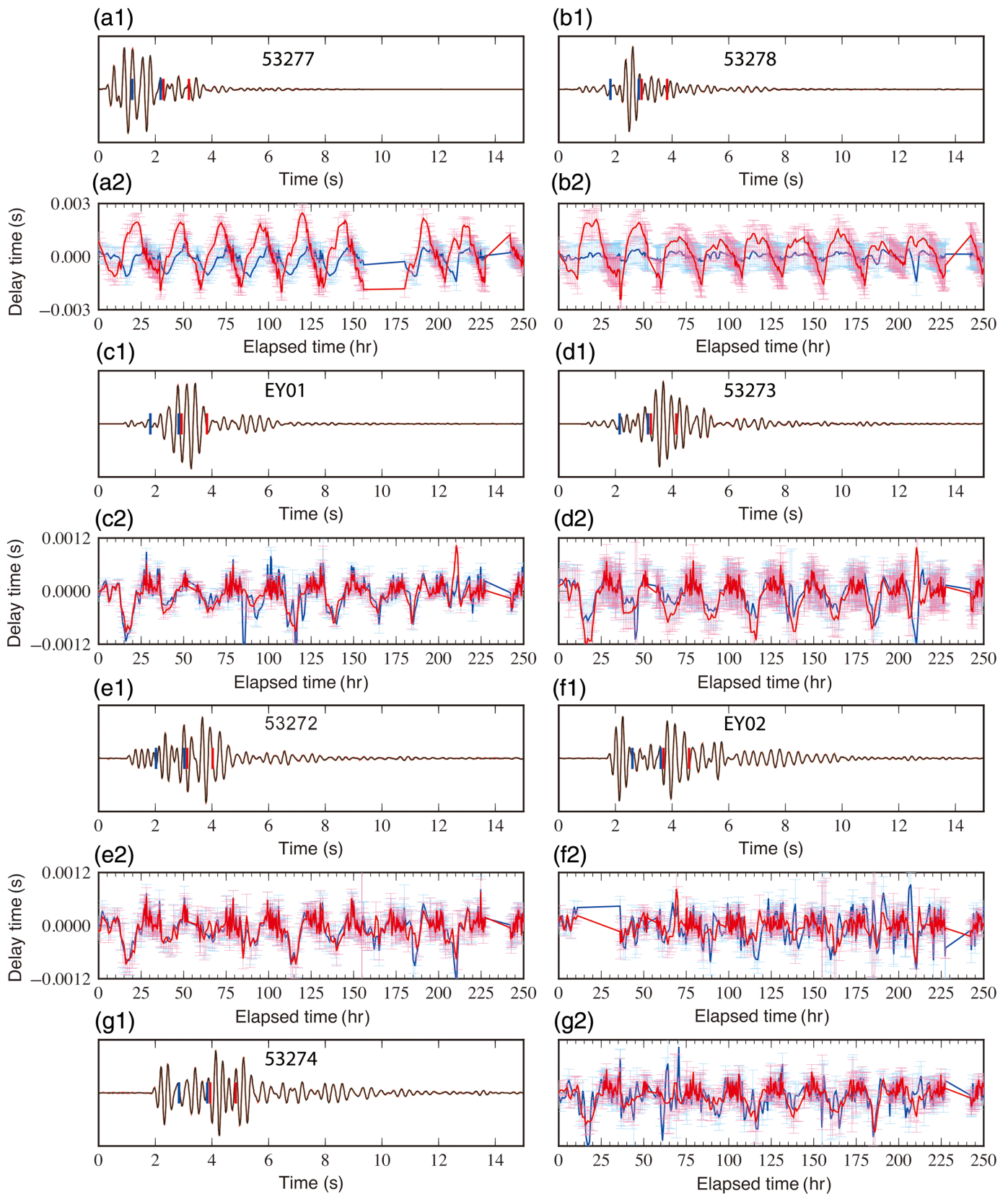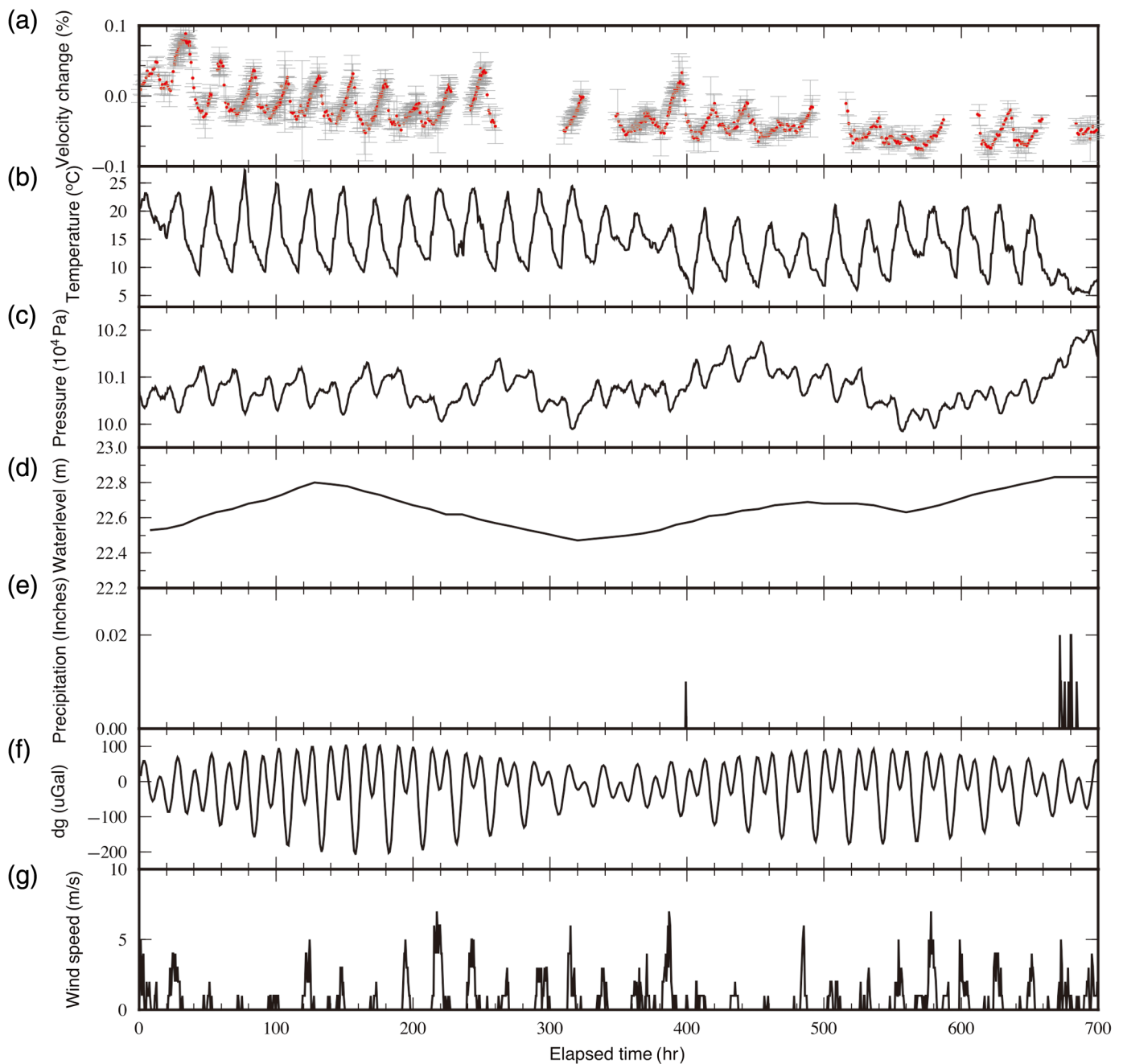
Figure 3. Air-gun signals (after deconvolution) of the near-offset stations including (a1) station 53277 (~700 m), (b1) station 53278 (~2.3 km), (c1) station EY01 (~3.4 km), (d1) station 53273 (~3.9 km), (e1) station 53272 (~5.3 km), (f1) station EY02 (~7.8 km), and (g1) station 53274 (~8.8 km); the blue and red line shows the window of measured delay time. (a2–g2) Measured delay time in different stations. The color version of this figure is available only in the electronic edition.

Figure 4. A comparison of the estimated delay time in station 53277 (~700 m) with (a) velocity change, (b) temperature, (c) barometric pressure, (d) water level of Dayindian reservoir, (e) precipitation, (f) synthetic solid earth tide, and (g) the wind speed. The good correlation between delay time and temperature is observed. The color version of this figure is available only in the electronic edition.

station 53273 (~3.9 km) (Fig. 7b). In addition, we observe a remarkable ~14 days' periodicity in most stations but not in the nearest stations, 53277 (~700 m) and 53278 (~2.3 km). The 14-day periodicity is corresponded to spring and neap tides, which was also observed in Yamamura *et al.* (2003). This may indicate that there exist potentially systematic relations between *dv/v* in farther away stations and the source mechanism that causes the observed velocity change.

Comparison of atmospheric data with *dv/v*

We divide the velocity changes together with the air pressure and temperature into different frequency components, including the long-term variations and daily variations using

the M-SSA method to do the signal decomposition and reconstruction (Fig. S4a,b).

From Figure S4a, the time series of air pressure show a strong, long-term trend (RCs 1 and 2), the five-day period change (RCs 3), daily variability (RCs 4 and 5), moderate
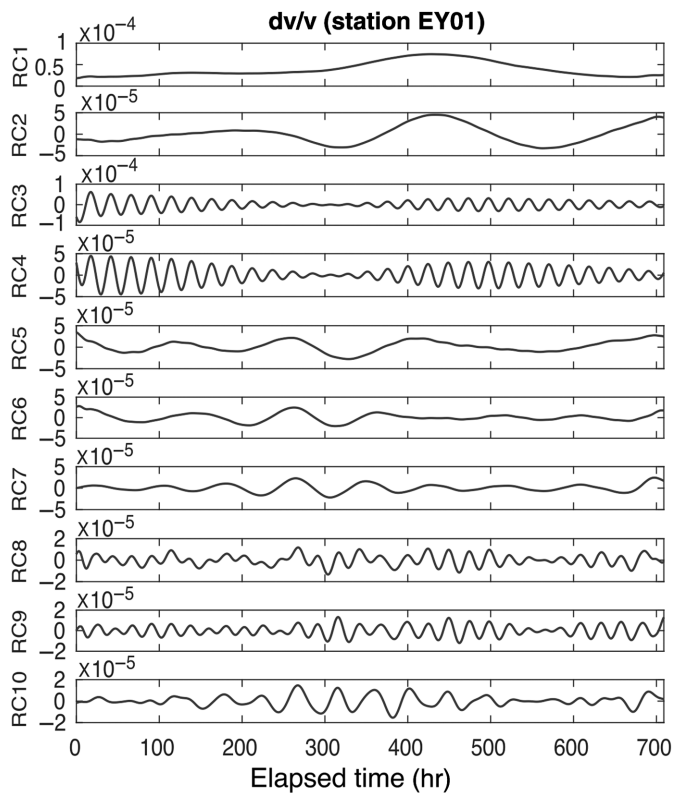
Figure 5. The reconstructed components (RCs) for seismic velocity change in broadband station EY01 (∼3.4 km) using the first 10 spatiotemporal principal components corresponding to the largest 10 eigenvalues.

semiannual variability (RCs 6 and 7), and no significant variability at other periods. Daily change of air pressure contributes a moderate portion of the whole air pressure variation (see Fig. S4a). According to Figure S4b, RCs 2 and 3 are mainly daily temperature signals that can be added up to ∼10 centigrade difference. In addition, it contains a strong, long-term trend (RCs 1 and 4) and semidiurnal changes (RCs 6) (see Fig. S4b). Here, the first 10 RCs are significant in that the cumulative percentage explained by the first 10 eigenvalues almost reaches 1 in the M-SSA of air pressure (100%), temperature (99.65%), and dv/v (74.59%) time series, which is enough for our research that focuses on the daily changes (see Figs. S5, S6).

For the semidiurnal component in air pressure and temperature, the highest possible interpretation would be tidal effects, and the main contributions would come from the M2 (28.98°/hr) and the S2 (30°/hr) components.

Figure 8a,b compares the daily velocity change in station 53277 (∼700 m) with the extracted daily air pressure and temperature changes. The air pressure time series (red curve) lag behind the dv/v time series (blue curve) for about 10 hr. The temperature changes (red curve) are around 5 hr ahead of the dv/v changes (blue curve).

Figure 8c,d compares the daily velocity change in station EY01 (∼3.4 km) with the extracted daily air pressure and temperature changes. The changes in daily seismic velocity show a clear dependence on air pressure, whereas the phase of velocity change and temperature is anticorrelated with 12 hr' phase lag.

The long-term velocity change (LTV) of broadband station EY01 (∼3.4 km) compared with atmospheric pressure and temperature changes is shown in Figure 9,b. It appears that the LTV agrees better in phase with the air pressure change. We found that the LTV is positively in phase with temperature change in the beginning. However, the phase turned opposite after 300 hr. The result indicates that the LTV of station EY01 (∼3.4 km) is more likely caused by air pressure. Besides, we observed a five-day cycle both in dv/v and air pressure time series, and the phases matched quite well (Fig. 9c). We do not find a five-day cycle in the temperature record.
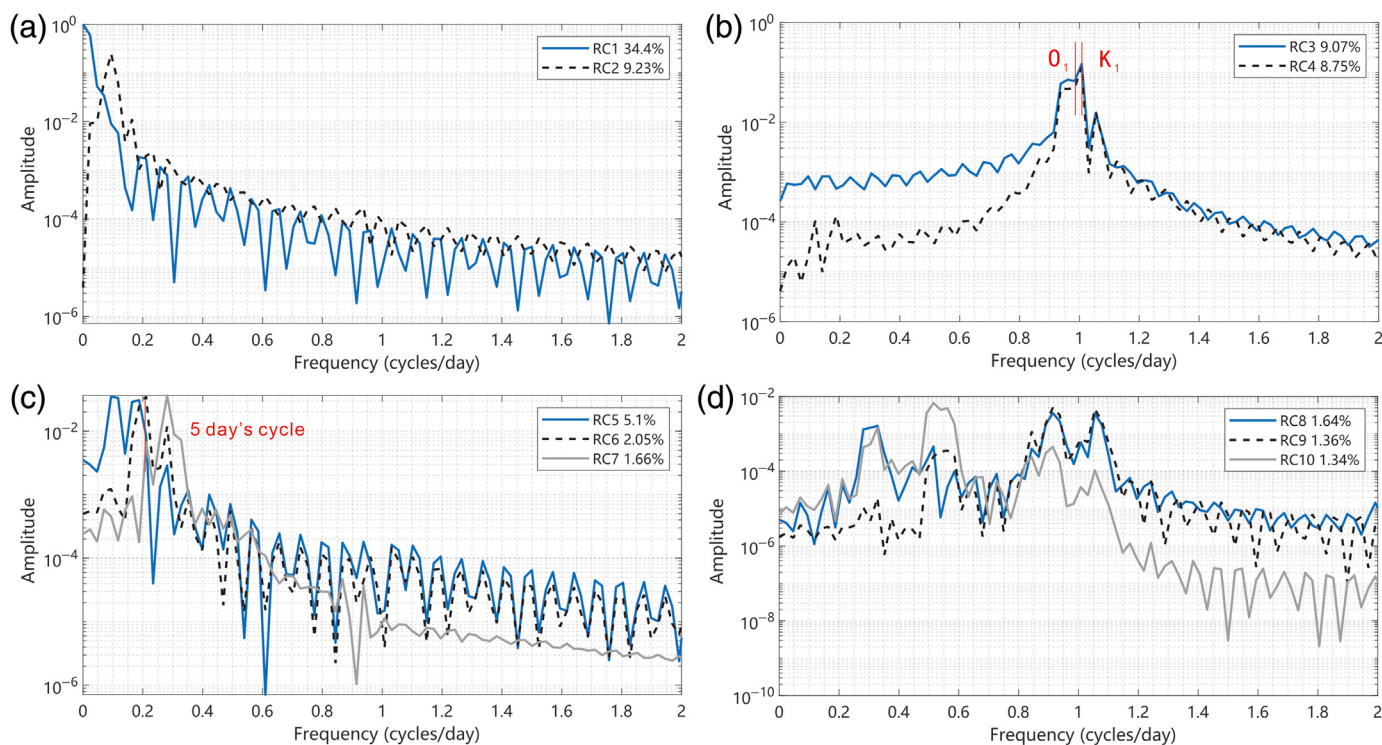
Discussion

Although there are not large dynamic stress perturbations during our one-month experiment period in this research area, the main factors that have been known to influence the seismic-velocity changes would be surface temperature changes, air pressure, and solid earth tide. The reason we did not consider the hydrological effects is that there was little rain, and the water level of the Dayindian reservoir varied little during the whole period. From the results we observed earlier, we suggest the main reasons that cause the velocity changes of the nearest stations 53277 (∼700 m) and 53278 (∼2.3 km) are different from the rest of other farther away stations.

As to the daily seismic-velocity variations, there were many researchers who argued that their measurements showed daily cycles that were well correlated with the temperature record. The reason varies from the instrument related auto-oscillations induced by temperature (Silver *et al.*, 2007; Niu *et al.*, 2008) and the real subsurface thermally induced strain change (Wang *et al.*, 2008, 2020; Richter *et al.*, 2014; Lu and Wen, 2017). In our case, the phase shift between the velocity change and the surface temperature curve excludes the possibility that the velocity changes are caused by technical effects due to the heating of the instruments (Sens-Schönfelder and Larose, 2008). The only mechanism that interprets the plausible lag between the observed dv/v signals and temperature variations is temperature-induced thermoelastic strain, so we infer this to be the dominant source of the observed velocity changes for at least two nearest stations (station 53277 [∼700 m] and station 53278 [∼2.3 km]). This interpretation is supported by the coherency between the dv/v of these stations and the temperature records, which is significantly and consistently higher compared with the coherency between the dv/v and other considered records.

In addition, there were former researchers who confirmed the tidal effect dominated velocity changes (e.g., Reasenberg and Aki, 1974; Liu *et al.*, 1983; Takano *et al.*, 2014; Hillers,

Figure 6. Relative power spectra of *dv/v* after applying Multichannel Singular Spectrum Analysis (M-SSA) method. (a) The spectra of the long-term *dv/v* shown as RC1 (blue line) and RC2 (black dashed line) components with contribution of 34.4% and 9.23%, respectively. (b) The spectra of daily *dv/v* shown as RC3 and RC4 components with total contribution of 17.82%. The two red bars mark the periods corresponding to two periods with tidal strains (O1 [25.819 hr] and K1 [23.934 hr]). (c) The spectra of the relative long-term *dv/v* shown as RC5 (blue line), RC6 (black dashed line), and RC7 (gray line) components. There is five days cycle in RC6 shown in red bar. (d) The spectra of three other components with less contribution as RC8 (1.64%), RC9 (1.36%), and RC10 (1.34%). The color version of this figure is available only in the electronic edition.

Retailleau, *et al.*, 2015). For the semidiurnal variation, the closest explanation would be tidal effects. In addition, we observe the semidiurnal and terdiurnal frequency components in the velocity changes of stations with different source–receiver distances (see Fig. S7). In station EY01 (∼3.4 km), the M-SSA method is able to detect the semidiurnal (RC12 and RC13) with a total contribution of 1.92% and terdiurnal signals (RC46 and RC49) with a total contribution of 0.41% (see Fig. S8). Because the temperature and air pressure effects are much more likely diurnal variation (see Fig. S7), in case the variation actually is due to earth tides, the main contributions would come from the M2 (1.932 c/day) and S2 (2.0 c/day) components (Bungum *et al.*, 1977). Takano *et al.* (2014) found that the amplitudes of the tidal strain vary from -2×10^{-8} to 3×10^{-8} of the dominant M2 component during their observation periods. Other researchers found that the tidal stress was nearly an order of magnitude smaller than changes in barometric pressure (Niu *et al.*, 2008; Wang *et al.*, 2008). Because the semidiurnal and terdiurnal components in our observed velocity changes are quite small, we do not consider the earth tides contribute the comparable magnitude of velocity change to that from the temperature and air pressure.

For the daily velocity changes obtained in farther away stations, we can consistently find that the amplitude of the velocity change reached the minimum at around 14 days. We believe the period of such signals may be larger than 14 days. However, the one-month data we used may not be enough to include the whole period of such signal. The stations 53277 (∼700 m) and 53278 (∼2.3 km) did not show this kind of signal

(Fig. 7). The cause for the half-month cycle is probably associated with the spring and neap tides. Because the wavepaths of the nearest two stations are quite shallow, the uppermost soft material is less affected by tidal strain. We will investigate the ∼14 days' periodicity with longer timespan data in future studies.

Considering the mean value of the maximum amplitude of *dv/v* for each cycle per day as the amplitude of velocity changes for each station, we find the estimated velocity changes generally decrease with increasing source–receiver distance, no matter for the results based on the raw *dv/v* (blue dots) or the extracted daily *dv/v* (green dots) (Fig. 10). It seems that the shallower the wave travels, the larger the velocity change is. The obviously high amplitude in station 53260 (∼4.7 km) was probably due to the local site effect, which is located in the LVZ formed by the Binchuan basin and the Chenghai fault.
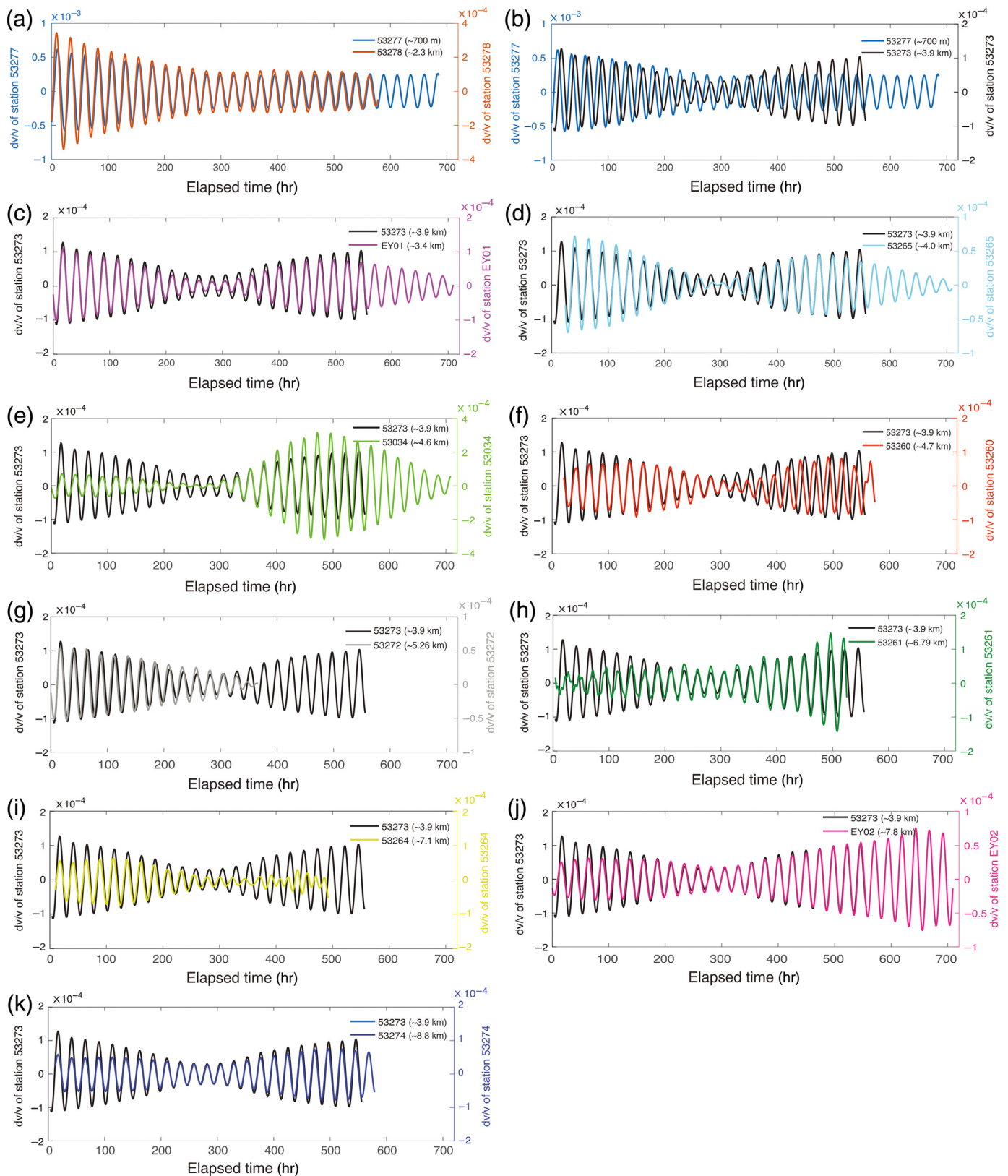
Figure 7. Comparison of the extracted daily velocity change using M-SSA in different stations with 2–3 s lapse time window. (a) *dv/v* between the nearest station 53277 (~700 m) and station 53278 (~2.3 km). (b–k) *dv/v* between the chosen reference station 53273 (~3.9 km) and other stations, namely station EY01 (~3.4 km), station 53265 (~4.0 km), station 53034 (~4.6 km), station 53260 (~4.7 km), station 53272 (~5.3 km), station 53261 (~6.8 km), station 53264 (~7.1 km), station EY02 (~7.8 km), and station 53274 (~8.8 km), respectively. The color version of this figure is available only in the electronic edition.

Figure 8. (a,b) Comparison of the daily seismic velocity changes in station 53277 (~700 m) with (a) air pressure and (b) surface temperature. (c,d) Comparison of the daily seismic velocity changes in station EY01 (~3.4 km) with (c) air pressure and (d) surface temperature. The color version of this figure is available only in the electronic edition.
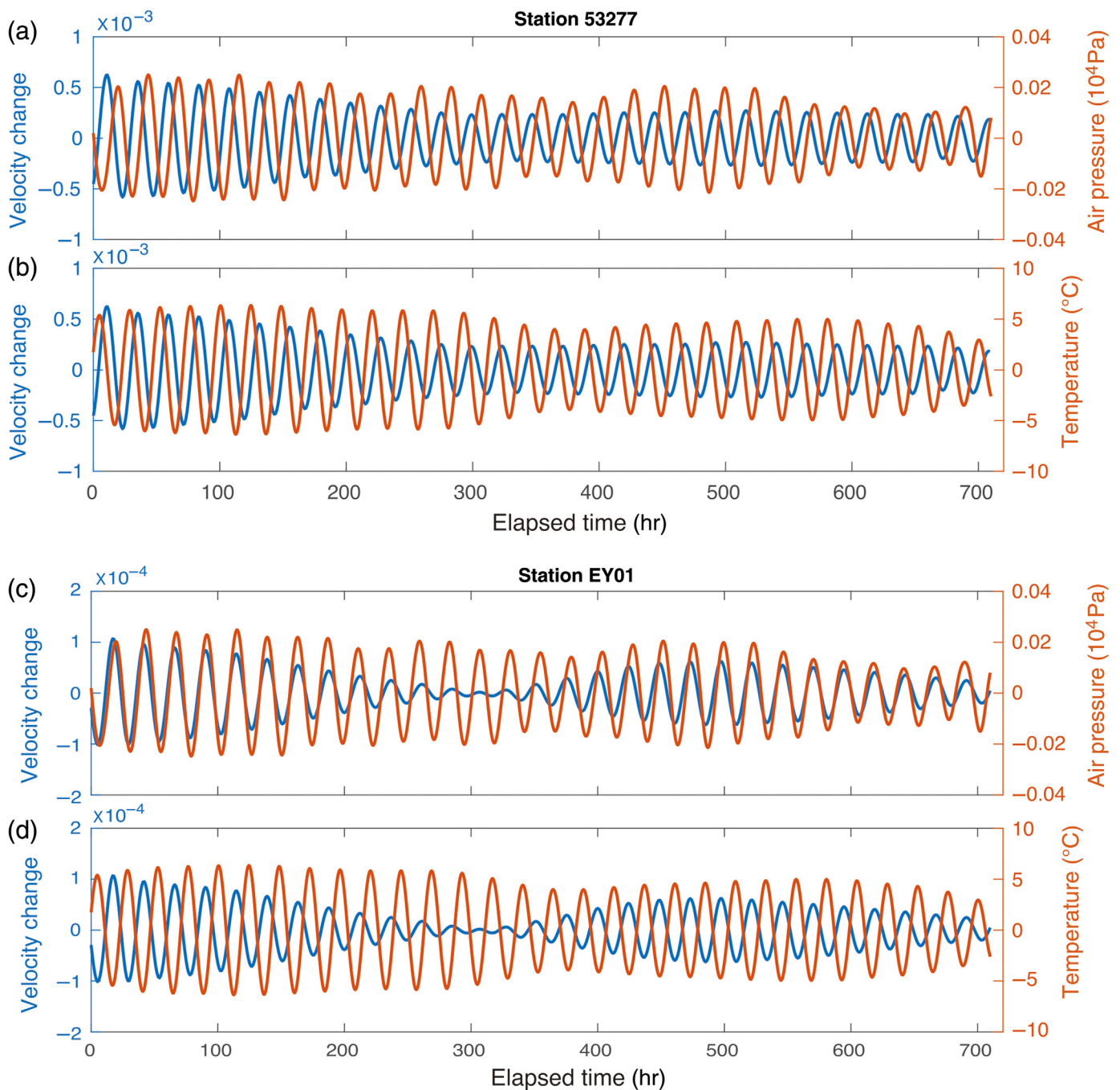
Effect of temperature

Ben-Zion and Allam (2013) estimated the thermoelastic strain ε_{xx} induced by 20°C temperature change with a spatial wavelength of 10 km, which was 2.7×10^{-7} at 0.5 km depth and 3.0×10^{-8} at 3 km depth.

Estimating the delay between the dv/v variations and temperature records (Fig. 8b,d) indicates that changes in seismic velocities lag consistently behind daily variations of the temperature field. The estimated delays in the nearest two stations (station 53277 [~700 m] and station 53278 [~2.3km]) follow a distribution that is centered at five hours (Figs. 7a and 8b). Although in farther away stations, the estimated delays are all beyond 12 hr (Figs. 7c–i and 8d). Because the temperature changes at different depths are not in phase, the temperature at the subsurface lags behind the temperature at the surface. For the daily temperature change, given that the frequency

Figure 9. Comparison of the long-term seismic velocity changes of station EY01 (~3.4 km) with (a) air pressure changes and (b) surface temperature changes. (c) Comparison of the five days' periodic seismic velocity changes of station EY01 (~3.4 km) with air pressure changes of similar frequency. The color version of this figure is available only in the electronic edition.
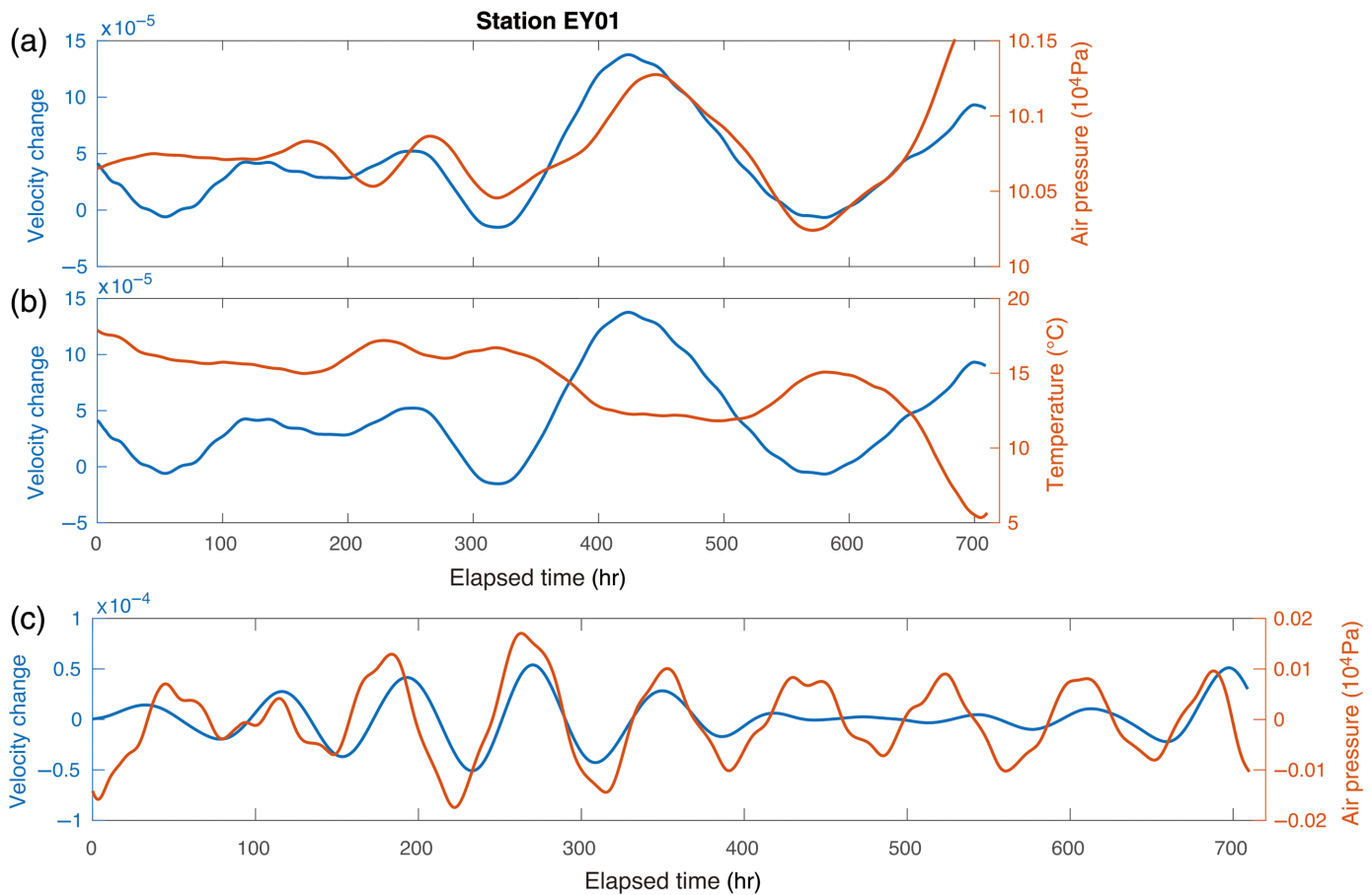
$\omega = 7.27 \times 10^{-5}$ rad s^{-1} and the thermal diffusivity $\kappa = 1$ mm^2 s^{-1}, then the skin depth is 0.17 m (according to equation [4.90] in Turcotte and Schubert, 2002), and the phase delay between the temperature change at the surface and at the skin depth is 1 rad (57.3°, about 3.82 hr, according to equation 4.91 in Turcotte and Schubert, 2002). Based on a dominant frequency of 3–5 Hz and a P-wave velocity of 2.8 km/s in our observed air-gun signals, we estimated the penetrating depth to be a few tens of meters for the nearest stations (~700 m source–receiver distance for station 53277 and ~2.3 km source–receiver distance for station 53278). Thus, it is possible for the five-hour delay between temperature and observed velocity change.

For thermoelastic-induced strains, to interpret the appreciable phase lag between temperature and induced strain, Ben-Zion and Leary (1986) bring about the "equivalent upper layer." This implies that if the observed strain or velocity change is to be explained by thermoelastic stress, the thermal input is not at the surface, but at a depth of y_b (equivalent upper layer), the material above acting as an insulator incapable of transmitting much stress (Ben-Zion and Leary, 1986; Tsai, 2011; Ben-Zion and Allam, 2013). Its thickness is given by $y_b = 2 \times \Delta t \sqrt{\pi \kappa / \tau}$, in which τ denotes the daily period; κ is the thermal diffusivity coefficient of soil, $\kappa = 2.16 \times 10^{-2}$ m^2/day; $\Delta t = 5$ hr is the delay time between

temperature and the velocity change. Thus, in our case, $y_b = 2 \times \frac{5}{24} \sqrt{\pi \times 2.16 \times 10^{-2}} = 0.1$ m.

However, the thermoelastic stress induced by temperature change cannot interpret the consistent phase delay of larger than 12 hr between farther away stations and temperature change. In contrast, the contribution of air pressure can, to some extent, explain the consistent phase of farther away stations (Figs. 7c–i and 8c).

Effect of air pressure

In addition to the thermoelastic effect induced by the temperature discussed earlier, air pressure produces a direct elastic loading effect that could also influence the velocity variation. As discussed by (Tsai, 2011), the direct loading effect will produce an instant strain variation to the subsurface structure. In addition, Hillers, Ben-Zion, et al. (2015) pointed out that the pressure-induced stress variations propagate with the
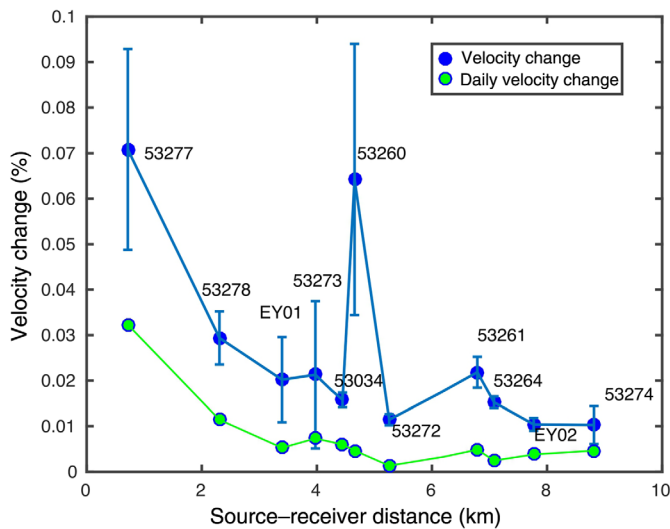
Figure 10. The relative velocity change (estimated from the mean value of the maximum velocity change in each cycle) with error bar as a function of source–receiver distance (blue dots). The green dots are daily velocity change (estimated from the mean value of the maximum velocity change in each cycle) derived from M-SSA method. The color version of this figure is available only in the electronic edition.

shear-wave speed, leading to near–instantaneous interactions. Because there is phase-to-phase coherence between the air pressure and the observed velocity change in farther away stations (Fig. 8c), we think the direct loading effect dominates the results of these stations. The strain due to the air pressure change is $\sim 8 \times 10^{-8}$ at the shallow layer (calculated using the software COMSOL). The loading strain from air pressure decays little with depth than thermoelastic strain, which means that with the increasing of the depth the direct loading strain effect dominates. This may at some point interpret the higher correlation between air pressure and the dv/v in farther away stations that have a deeper wavepath.

In our case, for the stations that the daily velocity changes have a high correlation and are in phase-to-phase with the air pressure change, we can see that its long-term velocity change also has good accordance with the air pressure change (Fig. 9a).

We thought that for the nearest two stations, because the penetrating depths of waves were shallow, the dominant influence of velocity change was from the thermoelastic effect induced by temperature rather than the loading effect from air pressure. For the farther away stations, the velocity changes were phase-to-phase with air pressure. This may indicate that due to the waves propagating further and deeper, thermoelastic strain decays quite fast with depth, which made the air pressure effect surpass the temperature effect for farther away stations.

Another phenomenon was that the velocity change was observed to decay with the distance (Fig. 10). Our measured velocity perturbation is an average of integrated velocity

changes occurring at different depths. As confining stress increases with depth, crack density decreases with depth, and, therefore, velocity perturbation should also decrease with depth.

The observed large velocity change must be related to the shallow depth that the waves have sampled. It may explain why the velocity perturbation varies significantly at a shallower depth and decreases with the source–receiver distance. For the stations with large amplitude velocity change, the reason is that these stations are within the Binchuan basin. In the east of the air-gun source, there locates the Chenghai fault and the Binchuan basin, of which the sediment thickness is larger than 500 m. The signal-to-noise ratios of the stations locate inside the Binchuan basin are relatively low, and it is hard to extract the daily variation for these stations.

Using the velocity changes and the barometric pressure change, we obtain a value of stress sensitivity of 10^{-6}/Pa. This value compares well with the values reported in the literature (Yamamura *et al.*, 2003).

Conclusion

In this study, we detect and quantify the seismic-velocity variations using air-gun source data with high-temporal resolution (~ 1 hr) and large spatial (~ 10 km) and time-length coverage (~ 1 month), which is more capable of high-resolution local-scale detection. By introducing the deconvolution method and the sliding window cross-correlation method, we can eliminate the intercepting time error and obtain a precision of 10^{-5} to 10^{-4} in measuring the velocity change. In addition, we use an advanced M-SSA technique to decompose dv/v time series as well as the environmental data to better understand the physical mechanism of the seismic-velocity change.

As a result, we observe a daily variation of $\sim 10^{-4}$ in the velocity perturbation. The daily-cycle velocity change of the two nearest stations, 53277 (~ 700 m) and 53278 (~ 2.3 km), track very well with 5.0 ± 1.5 hr delay with the temperature data. This indicates a high sensitivity of the subsurface velocity to temperature change in shallow layers, which can be interpreted by thermoelastic modeling. Besides, changes in barometric pressure are attributed to the velocity change in the farther away stations with phase-to-phase coherency. For long-period velocity change, the higher correlation with air pressure also verifies that the air pressure effect may be dominant for farther away stations. Furthermore, the amplitude of the velocity change decreases with source–receiver distance. The velocity changes in the shallow surface, as well as the sedimentary basin, are larger than velocity changes in the deeper depth.

Because the temperature and air pressure are ubiquitous, our method may provide a way to measure the property of rocks and shallow structures in situ. These measurements of the atmospheric response from air-gun signals may also be useful to quantitatively discuss observed seismic-velocity

changes associated with coseismic displacement and to understand the variations in the crustal structure.

Data and Resources

Declaration of Competing Interests

The authors acknowledge that there are no conflicts of interest recorded.

Acknowledgments

References

Ben-Zion, Y., and A. A. Allam (2013). Seasonal thermoelastic strain and postseismic effects in Parkfield borehole dilatometers, *Earth Planet. Sci. Lett.* **379,** 120–126, doi: 10.1016/j.epsl.2013.08.024.

Ben-Zion, Y., and P. Leary (1986). Thermoelastic strain in a half-space covered by unconsolidated material, *Bull. Seismol. Soc. Am.* **76,** 1447–1460.

Birch, F. (1960). The velocity of compressional waves in rocks to 10 kilobars, part 1, *J. Geophys. Res.* **65,** 1083–1102.

Birch, F. (1961). The velocity of compressional waves in rocks to 10 kilobars, part 2, *J. Geophys. Res.* **66,** 2199–2224.

Brenguier, F., M. Campillo, C. Hadziioannou, N. M. Shapiro, R. M. Nadeau, and E. Larose (2008). Postseismic relaxation along the San Andreas fault at Parkfield from continuous seismological observations, *Science* **321,** 1478–1481.

Brenguier, F., M. Campillo, T. Takeda, Y. Aoki, N. M. Shapiro, X. Briand, K. Emoto, and H. Miyake (2014). Mapping pressurized volcanic fluids from induced crustal seismic velocity drops, *Science* **345,** no. 6192, 80–82.

Bungum, H., T. Risbo, and E. Hjortenberg (1977). Precise continuous monitoring of seismic velocity variations and their possible connection to solid Earth tides, *J. Geophys. Res.* **82,** 5365–5373, doi: 10.1029/JB082i033p05365.

Carter, G. C. (1987). Coherence and time delay estimation, *Proc. IEEE* **75,** no. 2, 236–255, doi: 10.1109/PROC.1987.13723.

Chen, J. H., B. Froment, Q. Y. Liu, and M. Campillo (2010). Distribution of seismic wave speed changes associated with the 12 May 2008 Mw 7.9 Wenchuan earthquake: Wave speed changed by the Wenchuan earthquake, *Geophys. Res. Lett.* **37,** L18302, doi: 10.1029/2010GL044582.

Chen, M., W. Yang, W. T. Wang, B. S. Wang, H. K. Ge, L. Chen, Y. S. Ding, J. Y. Qiao, and Y. Chen (2014). Influencing factors of seismic signals generated by un-tuned large volume airgun array in a land reservoir, *Earthq. Sci.* **27,** 365–376, doi: 10.1007/s11589-014-0073-0.

Chen, Y., B. S. Wang, and H. J. Yao (2017). Seismic airgun exploration of continental crust structures, *Sci. China* **60,** no. 10, 1739–1751, doi: 10.1007/s11430-016-9096-6.

Clayton, R., and R. Wiggins (1976). Source shape estimation and deconvolution of teleseismic body wave, *Geophys. J. Roy. Astron. Soc.* **47,** 151–177.

Ghil, M., M. R. Allen, M. D. Dettinger, K. Ide, D. Kondrashov, M. E. Mann, A. W. Robertson, A. Saunders, Y. Tian, F. Varadi, et al. (2002). Advanced spectral methods for climatic time series, *Rev. Geophys.* **40,** 1003, doi: 10.1029/2000RG000092.

Haase, J. S., P. M. Shearer, and R. C. Aster (1995). Constraints on temporal variations in velocity near Anza, California, from analysis of similar event pairs, *Bull. Seismol. Soc. Am.* **85,** 194–206.

Hadziioannou, C., E. Larose, A. Baig, P. Roux, and M. Campillo (2011). Improving temporal resolution in ambient noise monitoring of seismic wave speed, *J. Geophys. Res.* **116,** no. B7, doi: 10.1029/2011JB008200.

Hillers, G., Y. Ben-Zion, M. Campillo, and D. Zigone (2015). Seasonal variations of seismic velocities in the San Jacinto fault area observed with ambient seismic noise, *Geophys. J. Int.* **202,** 920–932, doi: 10.1093/gji/ggv151.

Hillers, G., L. Retailleau, M. Campillo, A. Inbal, J. P. Ampuero, and T. Nishimura (2015). In situ observations of velocity changes in response to tidal deformation from analysis of the high-frequency ambient wavefield, *J. Geophys. Res.* **120,** no. 1, 210–225, doi: 10.1002/2014JB011318.

Jiang, X. H., S. Q. Hu, and H. F. Yang (2021). Depth extent and Vp/Vs of the Chenghai fault zone, Yunnan, China constrained from dense-array-based teleseismic receiver functions, *J. Geophys. Res.* **126,** no. 8, doi: 10.1029/2021JB022190.

Jiang, X. H., H. F. Yang, W. Yang, and W. T. Wang (2020). Crustal structure in the Binchuan basin of Yunnan constrained from receiver functions on a 2-D seismic dense array, *Earthq. Sci.* **33,** 264–272, doi: 10.29382/eqs-2020-0264-01.

Julian, B. R., and G. R. Foulger (2010). Time-dependent seismic tomography, *Geophys. J. Int.* **182,** 1327–1338, doi: 10.1111/j.1365-246X.2010.04668.x.

Keppenne, C. L., and M. Ghil (1993). Adaptive filtering and prediction of noisy multivariate signals: An application to subannual variability in atmospheric angular momentum, *Int. J. Bifurcat. Chaos.* **3,** 625–634, doi: 10.1142/S0218127493000520.

Koulakov, I., and C. A. Vargas (2018). Evolution of the magma conduit beneath the galeras volcano inferred from repeated seismic tomography, *Geophys. Res. Lett.* **45,** 7514–7522, doi: 10.1029/2018GL078850.

Leary, P. C., P. E. Malin, R. A. Phinney, T. Brocher, and R. VonCollin (1979). Systematic monitoring of millisecond travel time variations near Palmdale, California, *J. Geophys. Res.* **84,** 659–666.

Li, Y. G., J. E. Vidale, K. Aki, F. Xu, and T. Burdette (1998). Evidence of shallow fault zone strengthening after the 1992 M7.5 Landers, California, earthquake, *Science* **279,** 217–219, doi: 10.1126/science.279.5348.217.

Li, Y. G., J. E. Vidale, S. M. Day, D. D. Oglesby, and E. Cochran (2003). Postseismic fault healing on the rupture zone of the 1999 M 7.1 Hector Mine, California, earthquake, *Bull. Seismol. Soc. Am.* **93,** 854–869, doi: 10.1785/0120020131.

Ligorría, J. P., and C. J. Ammon (1999). Iterative deconvolution and receiver-function estimation, *Bull. Seismol. Soc. Am.* **89,** 1395–1400.

Liu, C. Y., H. F. Yang, B. S. Wang, and J. Yang (2021). Impacts of reservoir water level fluctuation on measuring seasonal seismic travel time changes in the Binchuan basin, Yunnan, China, *Rem. Sens.* **13,** 2421, doi: 10.3390/rs13122421.

Liu, H. P., R. E. Westerlund, and J. B. Fletcher (1983). Precise measurement of seismic traveltimes—Investigation of variation from tidal stress in shallow crust, *Geophys. Res. Lett.* **10,** 377–380, doi: 10.1029/GL010i005p00377.

Lu, Z., and L. X. Wen (2017). Abnormally strong daily-cycle S1 strain tide: Observation and physical mechanism, *J. Geophys. Res.* **122,** no. 10, 8525–8537, doi: 10.1002/2017JB014383.

Luan, Y., H. F. Yang, and B. S. Wang (2016). Large volume air-gun waveform data processing (I): Binchuan, Yunnan, *Earthq. Res. China.* **2,** 305–318.

Mordret, A., T. D. Mikesell, C. Harig, B. P. Lipovsky, and G. A. Prieto (2016). Monitoring southwest Greenland's ice sheet melt with ambient seismic noise, *Sci. Adv.* **2,** e1501538, doi: 10.1126/sciadv.1501538.

Niu, F. L., P. G. Silver, T. M. Daley, X. Cheng, and E. L. Majer (2008). Preseismic velocity changes observed from active source monitoring at the Parkfield SAFOD drill site, *Nature* **454,** 204–208.

Niu, F. L., P. G. Silver, R. M. Nadeau, and T. V. McEvilly (2003). Migration of seismic scatterers associated with the 1993 Parkfield aseismic transient event, *Nature* **426,** 544–548, doi: 10.1038/nature02151.

Nur, A. (1971). Effects of stress on velocity anisotropy in rocks with cracks, *J. Geophys. Res.* **76,** 2022–2034.

Patanè, D., G. Barberi, O. Cocina, P. D. Gori, and C. Chiarabba (2006). Time-resolved seismic tomography detects magma intrusions at Mount Etna, *Science* **313,** 821–823, doi: 10.1126/science.1127724.

Peng, Z. G., and Y. Ben-Zion (2006). Temporal changes of shallow seismic velocity around the Karadere-Duzce branch of the north Anatolian fault and strong ground motion, *Pure Appl. Geophys.* **163,** 567–599.

Penna, N. T., and M. P. Stewart (2003). Aliased tidal signatures in continuous GPS height time series, *Geophys. Res. Lett.* **30,** doi: 10.1029/2003GL018828.

Reasenberg, P., and K. Aki (1974). A precise, continuous measurement of seismic velocity for monitoring in situ stress, *J. Geophys. Res.* **79,** 399–406.

Richter, T., C. Sens-Schönfelder, R. Kind, and G. Asch (2014). Comprehensive observation and modeling of earthquake and temperature-related seismic velocity changes in northern Chile with passive image interferometry, *J. Geophys. Res.* **119,** 4747–4765, doi: 10.1002/2013JB010695.

Schaff, D. P., and G. C. Beroza (2004). Coseismic and postseismic velocity changes measured by repeating earthquakes, *J. Geophys. Res.* **109,** no. B10, doi: 10.1029/2004JB003011.

Sens-Schönfelder, C., and E. Larose (2008). Temporal changes in the lunar soil from correlation of diffuse vibrations, *Phys. Rev. E* **78,** no. 4, 045601.

Sens-Schönfelder, C., and U. Wegler (2006). Passive image interferometry and seasonal variations of seismic velocities at Marble Volcano, Indonesia, *Geophys. Res. Lett.* **33,** no. 21, L21302, doi: 10.1029/2006GL027797.

Silver, P. G., T. M. Daley, F. L. Niu, and E. L. Majer (2007). Active source monitoring of cross-well seismic travel time for stress-induced changes, *Bull. Seismol. Soc. Am.* **97,** no. 1B, 281–293.

Snieder, R., A. Grêt, H. Douma, and J. Scales (2002). Coda wave interferometry for estimating nonlinear behavior in seismic velocity, *Science* **295,** 2253–2255, doi: 10.1126/science.1070015.

Snieder, R., J. Sheiman, and R. Calvert (2006). Equivalence of the virtual-source method and wave-field deconvolution in seismic interferometry, *Phys. Rev. E* **73,** no. 6, 066620, doi: 10.1103/PhysRevE.73.066620.

Takano, T., T. Nishimura, H. Nakahara, Y. Ohta, and S. Tanaka (2014). Seismic velocity changes caused by the earth tide: Ambient noise correlation analyses of small-array data, *Geophys. Res. Lett.* **41,** no. 17, 6131–6136, doi: 10.1002/2014GL060690.

Tsai, V. C. (2011). A model for seasonal changes in GPS positions and seismic wave speeds due to thermoelastic and hydrologic variations, *J. Geophys. Res.* **116,** no. B4, doi: 10.1029/2010JB008156.

Turcotte, D. L., and G. Schubert (2002). *Geodynamics, Applications of Continuum Physics to Geological Problems*, Second Ed., Cambridge University Press, New York, New York.

Walwer, D., E. Calais, and M. Ghil (2016). Data-adaptive detection of transient deformation in geodetic networks, *J. Geophys. Res.* **121,** no. 3, 2129–2152, doi: 10.1002/2015JB012424.

Wang, E., B. C. Burchfiel, L. H. Royden, L. Z. Chen, J. S. Chen, W. X. Li, and Z. L. Chen (1998). *Late Cenozoic Xianshuihe-Xiaojiang, Red River, and Dali Fault Systems of Southwestern Sichuan and Central Yunnan, China*, Vol. 327, Geological Society of America, Boulder, Colorado, Special Paper, 1–108.

Wang, B. S., H. K. Ge, W. Yang, W. T. Wang, B. Wang, G. H. Wu, and Y. J. Su (2012). Transmitting seismic station monitors fault zone at depth, *Eos Trans. AGU* **93,** no. 5, 49–50.

Wang, B. S., W. Yang, W. T. Wang, J. Yang, X. B. Li, and B. Ye (2020). Diurnal and semidiurnal P- and S-wave velocity changes measured using an airgun source. *J. Geophys. Res.* **125,** e2019JB018218, doi: 10.1029/2019JB018218.

Wang, B. S., P. Zhu, Y. Chen, F. L. Niu, and B. Wang (2008). Continuous subsurface velocity measurement with coda wave interferometry, *J. Geophys. Res.* **113,** no. B12, doi: 10.1029/2007JB005023.

Wessel, P., W. H. F. Smith, R. Scharroo, J. Luis, and F. Wobbe (2013). Generic mapping tools: Improved version released, *Eos Trans. AGU* **94,** 409–410.

Xu, Y., K. D. Koper, R. Burlacu, R. B. Herrmann, and D. N. Li (2020). A new uniform moment tensor catalog for Yunnan, China, from January 2000 through December 2014, *Seismol. Res. Lett.* **91,** no. 2A, 891–900, doi: 10.1785/0220190242.

Yamamura, K., O. Sano, H. Utada, Y. Takei, S. Nakao, and Y. Fukao (2003). Long-term observation of in situ seismic velocity and attenuation, *J. Geophys. Res.* **108,** no. B6, doi: 10.1029/2002JB002005.

Yang, H. F. (2015). Recent advances in imaging crustal fault zones: A review, *Earthq. Sci.* **28,** 151–162, doi: 10.1007/s11589-015-0114-3.

Yang, H. F., Y. H. Duan, J. H. Song, X. H. Jiang, X. F. Tian, W. Yang, W. T. Wang, and J. Yang (2020). Fine structure of the Chenghai fault zone, Yunnan, China, constrained from teleseismic travel time and ambient noise tomography, *J. Geophys. Res.* **125,** e2020JB019565, doi: 10.1029/2020JB019565.

Yang, H. F., Y. H. Duan, J. H. Song, W. T. Wang, W. Yang, X. F. Tian, and B. S. Wang (2021). Illuminating high-resolution crustal fault zones and temporal changes using multi-scale dense arrays and airgun sources, *Earthq. Res. Adv.* doi: 10.19743/j.cnki.0891-4176.202101002.

Yang, H. F., Z. F. Li, Z. G. Peng, Y. Ben-Zion, and F. Vernon (2014). Low-velocity zones along the San Jacinto fault, southern California, from body waves recorded in dense linear arrays, *J. Geophys. Res.* **119,** no. 12, 8976–8990, doi: 10.1002/2014JB011548.

Yang, W., B. Wang, H. Ge, and S. Yuan (2018). Temporal variation of seismic wave velocity associated with groundwater level observed by downhole airgun near the Xiaojiang fault zone, *Seismol. Res. Lett.* doi: 10.1785/0220170282.

Zhang, B., L. Liu, S. A. Khan, T. van Dam, E. Z. Zhang, and Y. B. Yao (2017). Transient variations in glacial mass near Upernavik Isstrøm (west Greenland) detected by the combined use of GPS and GRACE data, *J. Geophys. Res.* **122,** no. 12, 10,626–10,642, doi: 10.1002/2017JB014529.

Zhang, Y. Y., Y. R. An, F. Long, G. H. Zhu, M. Qin, Y. S. Zhong, Q. Xu, and H. F. Yang (2021). Short-term foreshock and aftershock patterns of the 2021 Ms 6.4 Yangbi earthquake sequence, *Seismol. Res. Lett.* doi: 10.1785/0220210154.

Ziolkowski, A. (1970). A method for calculating the output pressure waveform from an air gun, *Geophys. J. Int.* **21,** 137–161, doi: 10.1111/j.1365-246X.1970.tb01773.x.